PAPER

Check for updates

Novel Janus XGa–PbP (X = S, Se) monolayers: excellent photocatalysts for overall water splitting

Khawla Chaoui, [ID] [ab] Warda Elaggoune, [ID] *[c] Luc Henrard, [ID] [b] Kamel Zanat [ID] [a] and Mohamed Achehboune [ID] [b]

The search for efficient and sustainable materials for solar-driven water splitting has intensified with the emergence of two-dimensional (2D) Janus structures. In this work, we theoretically design and explore two novel Janus monolayers, SGa–PbP and SeGa–PbP, using first-principles calculations. Our results reveal that both monolayers are dynamically, thermally, and mechanically stable, and exhibit direct band gaps (0.93 eV for SGa–PbP and 1.24 eV for SeGa–PbP) ideally suited for visible-light absorption. Impressively, these systems display strong optical absorption in the visible and ultraviolet regions, with absorption coefficients reaching 10^5 cm^{-1}. The asymmetric structure induces built-in electric fields that enhance charge separation, while the PbP surface provides active hydrogen adsorption sites with nearly optimal free energy $|\Delta G_{H^*}|$ values for hydrogen evolution. Most notably, the corrected solar-to-hydrogen conversion efficiencies reach 40.69% and 31.75% for SGa–PbP and SeGa–PbP, respectively-significantly surpassing many state-of-the-art 2D photocatalysts. These findings position XGa–PbP Janus monolayers as highly promising candidates for next-generation solar hydrogen production technologies.

1 Introduction

As the global energy crisis deepens and environmental degradation accelerates, the urgency to develop sustainable energy solutions has grown significantly. Among various alternatives, hydrogen has emerged as a compelling solution due to its high energy density (122 kJ g^{-1}) and zero-emission combustion, producing only water as a byproduct.[1–3] Photocatalytic water splitting, which harnesses solar energy to drive redox reactions, offers a green and scalable pathway for hydrogen generation,[4–7] with additional applicability in CO_2 reduction and pollutant degradation.

The water splitting process involves two critical half-reactions: the hydrogen evolution reaction (HER) and the oxygen evolution reaction (OER).[8] For a photocatalyst to be effective, it must meet stringent criteria: having a suitable band gap, proper alignment of the conduction and valence bands with water redox potentials, robust visible light absorption, and excellent charge carrier dynamics.[9] Since the pioneering work of Fujishima and Honda on TiO_2,[10] extensive research has been devoted to the engineering of advanced photocatalysts. Yet, many widely studied systems suffer from intrinsic limitations,

such as subpar light absorption (*e.g.*, TiO_2,[11] $La_2Ti_2O_7$ (ref. 12)), high electron–hole recombination rates (*e.g.*, g-C_3N_4 (ref. 13)), or inadequate redox potential and catalytic activity (*e.g.*, Ag_3PO_4,[14] La-doped $NaTaO_3$ (ref. 15)). These deficiencies hinder their practical implementation.

The advent of two-dimensional (2D) materials has ushered in a new era for photocatalyst design.[16–19] Due to their atomic-scale thickness, 2D materials offer exceptional surface-to-volume ratios, providing a high density of catalytically active sites.[20] Their reduced dimensionality also improves the mobility of the charge carrier by shortening diffusion paths[21] and prolonging carrier lifetimes.[22] Moreover, their optoelectronic properties are highly tunable *via* strain engineering, surface functionalization, and layer number modulation, enabling efficient use of solar spectrum.[23]

Among the expanding library of 2D materials, Janus monolayers have emerged as front-runners for next-generation photocatalysts. Their hallmark feature, structural asymmetry across the atomic plane, induces a built-in out-of-plane dipole moment, giving rise to an intrinsic built-in electric field that promotes directional charge separation and improves carrier mobility.[24,25] This self-generated electric field can alleviate the strict requirement of a 1.23 eV band gap for water splitting, while simultaneously improving the catalytic activities of both HER and OER.[26] The experimental realisation of Janus transition metal dichalcogenides (TMDs), such as MoSSe,[27] has substantiated their superior photocatalytic performance. In parallel, theoretical studies on Janus structures like B_2P_6 (ref. 28) and M_2X_3 (M = Al, Ga, In; X = S, Se, Te)[21] have reported

[a]Guelma Physics Laboratory (GPL), Université 8 Mai 1945, BP 401, Guelma, Algeria. E-mail: chaoui.khawla@univ-guelma.dz

[b]Department of Physics, Institute of Structured Matter (NISM), University of Namur, Rue de Bruxelles 61, 5000, Namur, Belgium

[c]Laboratoire de Physique des Matériaux (L2PM), Faculté des Mathématiques, de l'informatique et des Sciences de la Matière, Université 8 Mai 1945, BP 401, Guelma, Algeria. E-mail: elaggoune.warda@univ-guelma.dz

solar-to-hydrogen conversion efficiencies exceeding the conventional limit 18%. Notably, Janus VI–III monolayers (VI = S, Se, Te; III = Ga, In)[29] demonstrate markedly improved charge separation compared to their symmetric analogs,[30] further underscoring the advantages of Janus engineering.

In this context, a novel subclass of 2D materials, Janus V–IV–III–VI monolayers, has recently garnered interest due to their unique structural complexity and tunable properties. These materials feature four atomically thin sublayers stacked in a sequence of V–IV–III–VI and crystallize in a non-centrosymmetric structure with inherent out-of-plane asymmetry. Lin et al.[31] initially proposed the V–IV–III–VI architecture (V = N, P; IV = Si, Ge, Sn; III = Al, Ga, In; VI = O, S), showing that many candidates exhibit thermodynamic and kinetic stability. Subsequently, Hu et al.[32] reported that XM–GaS monolayers (X = N, P; M = Si, Ge, Sn) are not only stable but also optoelectronically ideal for photocatalysis; specifically, SiP–GaS and GeP–GaS were found to possess suitable band alignments and visible light absorption exceeding 10^5 cm^{-1}. The complementary work by Deng et al.[33] on InSe–MQ systems (M = Si, Ge, Sn; Q = P, As) further validated the viability of this family, although some members (e.g., InSe–SiP) lacked the necessary redox potential under acidic conditions.

From an experimental perspective, unlocking the potential of Janus V–IV–III–VI monolayers hinges on adapting synthesis strategies proven for related layered chalcogenides. The foundational step would involve the synthesis of bulk symmetric V–IV–III–VI compounds, which can be achieved through well-established methods like chemical vapor transport (CVT)[34] and flux-assisted solid-state reactions.[35] Following bulk growth, mechanical or liquid-phase exfoliation could be used to obtain few-layer sheets, a standard procedure for isolating 2D materials from their bulk precursors. Alternatively, Janus asymmetry could be introduced by starting with a symmetric monolayer and employing selective top-layer substitution via a plasma-assisted chalcogen exchange, as successfully demonstrated in the synthesis of Janus MoSSe.[27] A more direct approach could utilize advanced deposition techniques like molecular beam epitaxy (MBE) or chemical vapor deposition (CVD), which allow for layer-by-layer assembly with sequential flux control to build the V–IV–III–VI structure.[36,37] Lastly, a scalable and cost-effective method like hydrothermal synthesis, which has been effectively used for creating other layered nanomaterials like g-C$_3$N$_4$,[38] could also be explored using appropriate precursors.

Despite recent advances, the elemental diversity within the V–IV–III–VI Janus monolayer family remains substantially underexplored, particularly regarding their potential in photocatalytic water splitting. In this study, we broaden this compositional space by introducing lead (Pb) as the group-IV constituent and design two novel Janus systems: SGa–PbP and SeGa–PbP. These Janus monolayers exploit the intrinsic stability and photocatalytic performance of XGa mono-chalcogenides (X = S, Se),[30,39] while incorporating the distinctive electronic characteristics of PbP. Although pristine PbP monolayers have previously been considered unsuitable due to their inadequate band gaps for overall water splitting under various pH conditions,[40] our results demonstrate that Janus engineering through XGa functionalization significantly enhances their photocatalytic potential. Both SGa–PbP and SeGa–PbP exhibit suitable band gaps, band edge alignments compatible with water redox potentials, strong visible-light absorption, and excellent conversion efficiencies-features critical for efficient solar-driven water splitting.

This study not only adds two novel members to the V–IV–III–VI Janus monolayer family, but also provides clear evidence that Janus engineering markedly improves photocatalytic efficiency.

2 Computational details

Density functional theory (DFT) calculations were performed using the Vienna Ab initio Simulation Package (VASP, version 6.3).[41,42] The exchange–correlation functional was treated using the Perdew–Burke–Ernzerhof (PBE) form of the generalized gradient approximation (GGA),[43,44] and the interactions between valence electrons and ion cores were described using the projector augmented wave (PAW) method.[45] To obtain more accurate electronic properties, calculations were also carried out using the Heyd–Scuseria–Ernzerhof hybrid functional (HSE06).[46] Optical properties were calculated using the non-interacting electron approximation. The hybrid HSE06 functional was also employed. The imaginary part of the dielectric function was computed from interband transitions, while the real part was derived via the Kramers–Kronig transformation.[47] A kinetic energy cutoff of 500 eV was used for the plane-wave basis set. The Brillouin zone was sampled using a Monkhorst–Pack k-point mesh of $12 \times 12 \times 1$. Structural relaxations were performed until the forces on each atom were less than 0.01 eV Å^{-1} and the total energy was converged to 10^{-6} eV. A vacuum layer of 25 Å was used along the z-direction to eliminate interactions between periodic images. van der Waals interactions were included using the DFT-D3 method with Becke–Johnson damping.[48] Dipole corrections were also applied in the work function calculations to account for the built-in dipole moment of the Janus monolayers. The dynamic stability of the structure was confirmed by phonon dispersion calculations using density functional perturbation theory (DFPT) on a $3 \times 3 \times 1$ supercell, with an energy convergence criterion of 10^{-9} eV.[49] Phonon spectra were generated using the PHONOPY code.[50,51] Thermal stability was evaluated using ab initio molecular dynamics (AIMD) simulations at 300 K for 7 ps with a time step of 1 fs, using the Nose thermostat.[52,53] Post-processing of VASP output was carried out using VASPKIT,[54] and structural and charge density visualisations were generated using VESTA.[55]

3 Results and discussions

3.1 Structural properties and stability

The Janus XGa–PbP (X = S, Se) monolayers were constructed by combining atomic sublayers extracted from their respective parent compounds: Pb$_2$P$_2$ and X$_2$Ga$_2$ (X = S, Se). Both parent materials exhibit layered architectures composed of four atomic planes and crystallize in the C_{3v} symmetry group. Specifically, a XGa layer from X$_2$Ga$_2$ and a PbP layer from Pb$_2$P$_2$ were assembled in an asymmetric fashion to form the Janus

configuration. This asymmetric stacking breaks the mirror symmetry with respect to the central plane of the parent monolayers, resulting in a built-in structural polarity along the z-direction. Fig. 1 provides a visual breakdown: the top panel shows side views of the parent monolayers, the middle illustrates the relaxed Janus structure from the side, and the bottom panels depict the top and bottom views, underlining the broken inversion symmetry, a characteristic feature of Janus systems.

The structural details, including optimised lattice constants, bond lengths, and layer thicknesses, are presented in Table 1. A progressive increase in these parameters is observed when moving from the S-based (SGa–PbP) to the Se-based (SeGa–PbP) systems. This trend is mainly attributed to the larger atomic radius of Se compared to S, consistent with structural behaviour in similar systems.[56–59]

The structural stability of the Janus XGa–PbP (X = S, Se) monolayers was examined by calculating their cohesive energy. This metric reflects the energy required to disassemble the material into its isolated atoms, providing a reliable indication of its energetic robustness. The cohesive energy per atom was obtained using the following expression:[56,59]

$$E_{\mathrm{coh}} = (E_{\mathrm{XGa-PbP}} - E_{\mathrm{Ga}} - E_{\mathrm{Pb}} - E_{\mathrm{P}} - E_{\mathrm{X}})/4 \tag{1}$$

where $E_{\mathrm{XGa-PbP}}$ denotes the total energy of the fully relaxed monolayer, and E_{Ga}, E_{Pb}, E_{P}, and E_{X} are the respective energies of the free-standing Ga, Pb, P, and chalcogen (S or Se) atoms. A more negative cohesive energy indicates stronger interatomic bonding, and thus greater stability of the monolayer. As presented in Table 1, all the calculated cohesive energies are negative, confirming the favourable binding and structural integrity of these systems.

To gain deeper insights into the stability of the proposed Janus monolayers, we performed phonon dispersion analyzes to probe their dynamical behavior. As depicted in Fig. 2(a) and (b),

Table 1 The calculated lattice constant a, thickness h, bond lengths d, and cohesive energy E_{coh} of the SGa–PbP and SeGa–PbP monolayers

System	a (Å)	h (Å)	$d_{\mathrm{Ga-Pb}}$ (Å)	$d_{\mathrm{Ga-X}}$ (Å)	$d_{\mathrm{Pb-P}}$ (Å)	E_{coh} (eV)
SGa–PbP	3.87	4.96	2.71	2.43	2.58	−3.15
SeGa–PbP	3.95	5.07	2.71	2.54	2.60	−3.04

the phonon spectra for both SGa–PbP and SeGa–PbP reveal entirely real (positive) vibrational frequencies throughout the Brillouin zone, particularly along the selected high-symmetry paths. The absence of imaginary phonon branches is a clear indication that both monolayers are dynamically stable in their relaxed configurations.

To further probe the thermal resilience of the Janus monolayers, *ab initio* molecular dynamics (AIMD) simulations were performed at 300 K for a total simulation time of 7 picoseconds. The evolution of total energy and system temperature for both SGa–PbP and SeGa–PbP is displayed in Fig. 2(c) and (d). The results reveal minor fluctuations in energy and temperature, with no signs of atomic diffusion, bond dissociation, or structural rearrangement throughout the simulation period. This confirms that both configurations remain thermally stable under ambient thermal conditions, reinforcing their promise for realistic operational environments.

3.2 Mechanical properties

The in-plane elastic properties of the XGa–PbP Janus monolayers were evaluated using the strain–stress method, a reliable method to probe the mechanical behaviour at the atomic scale. In this method, a series of small uniaxial and biaxial strains ranging from −1.5% to 1.5% were applied in steps of 0.005.

Given that XGa–PbP monolayers adopt hexagonal crystal symmetry, only two independent elastic constants, namely C_{11}
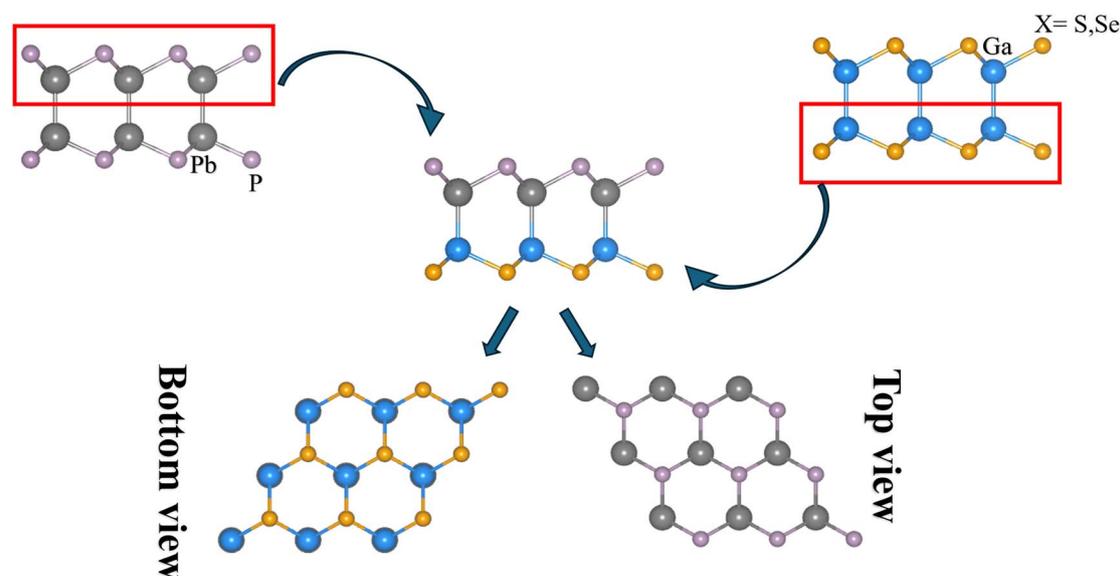

Fig. 1 Top panel: side views of the parent monolayers. Middle panel: side view of the relaxed Janus structure. Bottom panels: top and bottom views of the XGa–PbP Janus monolayer, highlighting the broken inversion symmetry characteristic of Janus systems.
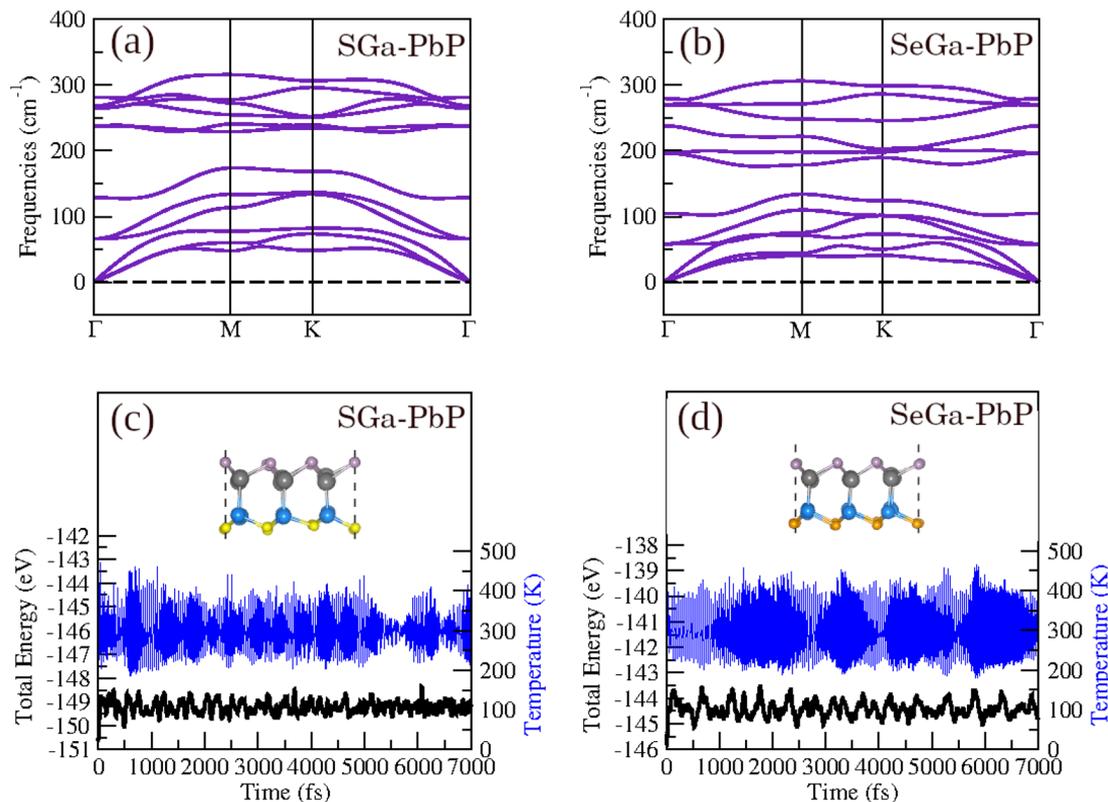
Fig. 2 (a and b) Phonon dispersion curves of the SGa–PbP and SeGa–PbP Janus monolayers, respectively. (c and d) *Ab initio* molecular dynamics (AIMD) simulations showing the total energy (black) and temperature fluctuations (blue) of the SGa–PbP and SeGa–PbP monolayers at 300 K.

and C_{12}, are sufficient to fully describe their mechanical response in the plane. These constants represent the stiffness of the material under longitudinal and transverse deformation, respectively. The mechanical stability of the monolayers was assessed according to Born criteria,[60,61] which define the necessary conditions for the elastic stability of hexagonal systems as:

$$C_{11} > 0, C_{11} > |C_{12}| \qquad (2)$$

These criteria ensure that the structure resists both tensile and shear perturbations. As summarised in Table 2, both SGa–PbP and SeGa–PbP monolayers satisfy these conditions, confirming their mechanical stability.

Additionally, from the elastic constants obtained, we calculated the key mechanical indicators:[62,63]

• Young's modulus

$$Y = \frac{C_{11}^2 - C_{12}^2}{C_{11}},$$

• Shear modulus

$$G = \frac{C_{11} - C_{12}}{2},$$

• Poisson's ratio

$$\nu = \frac{C_{12}}{C_{11}},$$

Both monolayers exhibit comparable mechanical properties, with only slight differences between them (Table 2). The SGa–PbP monolayer shows a slightly higher Young's modulus ($Y = 59.04$ N m^{-1}) and shear modulus ($G = 24.18$ N m^{-1}) compared to SeGa–PbP ($Y = 56.99$ N m^{-1}, $G = 23.30$ N m^{-1}). This indicates that SGa–PbP is marginally stiffer and more resistant to in-plane deformation than SeGa–PbP.

The Poisson's ratio for both materials is identical ($\nu = 0.22$), suggesting a similar tendency to undergo lateral contraction when stretched. This moderate Poisson ratio reflects a balanced mechanical response-neither brittle nor too ductile-which is desirable for many applications involving flexible or stretchable electronics.

Overall, both SGa–PbP and SeGa–PbP demonstrate good mechanical stability and flexibility. The slightly superior mechanical strength of SGa–PbP may offer an advantage in environments that require greater durability.

Table 2 Elastic constants C_{ij}, Young's modulus (Y), shear modulus (G) and Poisson's ratio (ν) of the SGa–PbP and SeGa–PbP monolayers

System	C_{11}	C_{12}	Y (N m^{-1})	G (N m^{-1})	ν
SGa–PbP	62.06	13.69	59.04	24.18	0.22
SeGa–PbP	59.96	13.35	56.99	23.30	0.22

3.3 Electronic properties

The electronic band structures of the Janus monolayers SGa–PbP and SeGa–PbP were calculated using both the PBE and the hybrid HSE06 functionals, the latter being known to provide reliable estimations of band gaps.[64] As depicted in Fig. 3, both monolayers exhibit direct band gaps located at the Γ point of the Brillouin zone, an electronic feature that is highly desirable for optoelectronic device applications. Within the PBE framework, the band gaps are found to be 0.42 eV for SGa–PbP and 0.66 eV for SeGa–PbP. The more accurate HSE06 functional predicts slightly larger values of 0.93 eV and 1.24 eV for SGa–PbP and SeGa–PbP, respectively. The increase in the band gap upon the substitution of sulfur with selenium reflects the influence of the atomic composition on the electronic structure and suggests a degree of band gap tunability.

The existence of a direct band gap in both systems facilitates efficient electron–hole pair generation and recombination, which is critical for high-performance applications in photovoltaics, photocatalysis, and light-emitting devices.[59,65,66] Moreover, the moderate band gap values indicate that these materials are suitable for operation under visible to near-infrared light, depending on specific device requirements.

To assess the possible influence of spin–orbit coupling (SOC) on the electronic properties, we performed additional PBE + SOC calculations (Fig. S1 and Table S1 in SI). The results show that the band gap differs from the PBE value by only 0.05 eV for SGa–PbP and 0.08 eV for SeGa–PbP. According to Borlido *et al.*[67] the average absolute error in band gap predictions due to pseudopotential choices or methodological inconsistencies is about 0.1 eV, which means that our observed differences lie within the typical numerical uncertainty of DFT methods. This suggests that SOC has only a weak energy splitting effect on the band structure in this system.[68,69] Furthermore, Huhn and Blum[70] reported that SOC-induced modifications to the band gap are of similar magnitude for both PBE and hybrid functionals such as HSE06, and can even be smaller in some cases with HSE06. Therefore, given that the largest shift we observe is

0.08 eV, including SOC in the HSE06 calculations would not be expected to change the qualitative trends or conclusions of this work.

Understanding carrier mobility is essential for assessing the suitability of materials for a range of applications, including photovoltaic and photocatalytic systems, particularly under conditions that require rapid charge transport. Since carrier mobility is inversely proportional to the effective mass, we computed the effective masses of electrons (m_e^*) and holes (m_h^*) for the SGa–PbP and SeGa–PbP Janus monolayers using their electronic band structures.

The effective masses were determined by fitting a parabolic function to the energy bands near the conduction band minimum (CBM) and the valence band maximum (VBM), based on the standard relation:[71]

$$m^* = \pm \frac{\hbar^2}{\dfrac{d^2 E(k)}{dk^2}} \qquad (3)$$

In this equation, $E(k)$ denotes the energy dispersion near the band edges, and k is the wavevector within the first Brillouin zone. For SGa–PbP, the effective electron mass of $m_e^* = 0.25$, m_0 and the effective hole mass of $m_h^* = 0.58$, m_0 suggest that electrons are more mobile than holes, which can lead to electron-dominated transport in optoelectronic applications. The relatively moderate hole effective mass still permits efficient transport, but with somewhat reduced mobility compared to electrons.

In contrast, the SeGa–PbP monolayer exhibits an even lower electron effective mass of $m_e^* = 0.19$, m_0, indicating enhanced electron mobility, while the hole effective mass remains comparable at $m_h^* = 0.59$, m_0. This further strengthens the potential of SeGa–PbP for fast electron transport, making it especially attractive for photocatalytic and photovoltaic systems, where rapid charge extraction and reduced recombination are critical for high performance. Moreover, the relatively small effective masses observed in both monolayers point
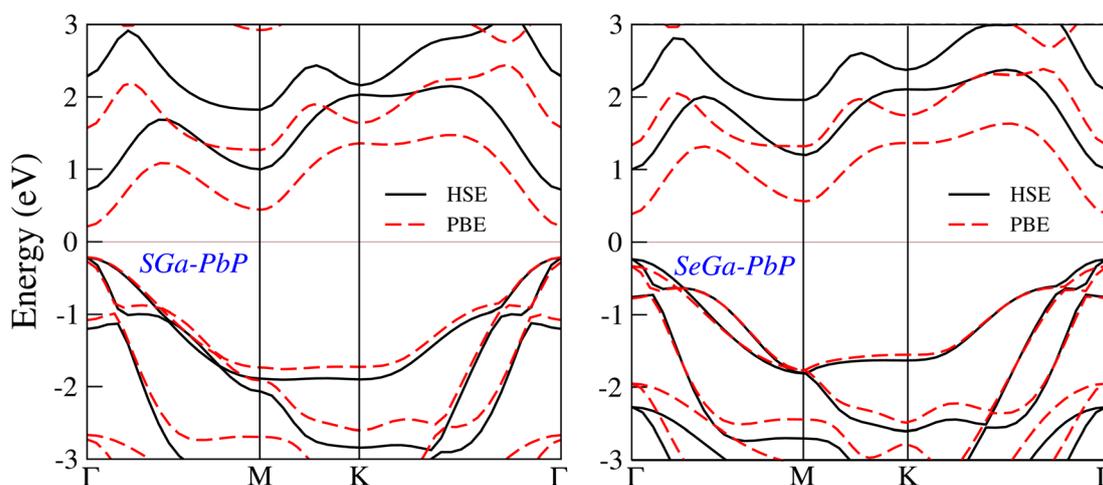

Fig. 3 Electronic band structures of the SGa–PbP and SeGa–PbP Janus monolayers, respectively, calculated using the PBE and HSE06 functional.

to low carrier inertia, which supports efficient charge carrier acceleration under an external field.

To further evaluate the efficiency of charge separation, we computed the separation efficiency parameter (R), defined as the ratio between the effective masses of the hole and the electron:[72,73]

$$R = \frac{m_h^*}{m_e^*} \tag{4}$$

A higher value of R indicates a more pronounced disparity between the electron and hole mobilities, which facilitates the spatial separation of the photogenerated charge carriers. This behaviour is beneficial in suppressing electron–hole recombination and, consequently, in improving the overall efficiency of the photocatalytic process.

As reported in Table 3, the calculated values of R are 2.32 for SGa–PbP and 3.10 for SeGa–PbP, confirming that both monolayers exhibit favourable charge separation characteristics. In particular, the higher value of R in SeGa–PbP suggests an even stronger separation tendency, further strengthening its potential for solar-driven and photocatalytic energy applications.

3.4 Optical properties

Maximizing solar energy utilisation is crucial to enhancing the photocatalytic efficiency of materials. To evaluate the light-harvesting capabilities of Janus SGa–PbP and SeGa–PbP monolayers, their optical absorption coefficients were calculated using the HSE06 hybrid functional, which offers a reliable description of electronic transitions.

The absorption coefficient, denoted as $\alpha(\omega)$, was determined using the following expression:[74]

$$\alpha(\omega) = \frac{\sqrt{2}\omega}{c} \sqrt{\sqrt{\varepsilon_1(\omega)^2 + \varepsilon_2(\omega)^2} - \varepsilon_1(\omega)} \tag{5}$$

where $\varepsilon(\omega) = \varepsilon_1(\omega) + i\varepsilon_2(\omega)$ is the complex dielectric function derived from the macroscopic response of the system, and c is the speed of light in vacuum.

As shown in Fig. 4, both the SGa–PbP and SeGa–PbP Janus monolayers exhibit pronounced optical absorption spanning the visible to ultraviolet (UV) regions. The absorption onset, occurring near 1 eV, corresponds closely to their computed band gaps—0.93 eV for SGa–PbP and 1.24 eV for SeGa–PbP—validating the direct transition nature of their electronic structures.

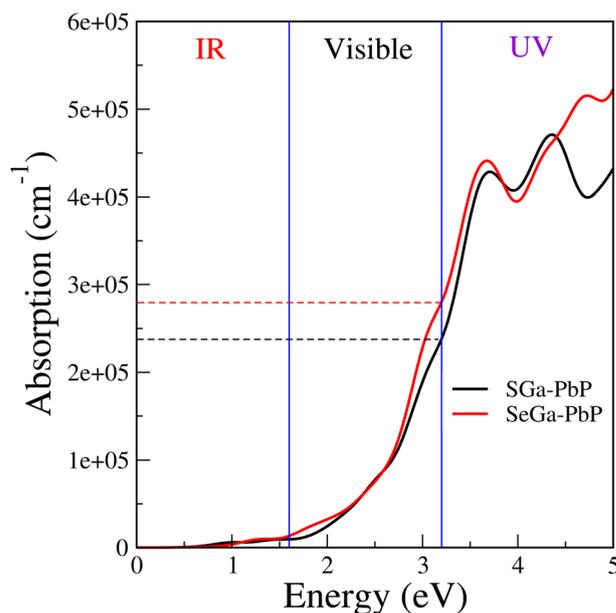Following onset, the absorption coefficient increases rapidly and reaches peak values of approximately 2.3 ×

Fig. 4 Optical absorption spectra of the SGa–PbP and SeGa–PbP Janus monolayers, respectively, calculated using the HSE06 functional.

10^5 cm^{-1} around 3.2 eV within the visible range. This pronounced optical response signifies strong photon–matter interaction and highlights the materials' suitability for harvesting solar energy. Compared to well-studied Janus and layered materials such as WSSe, MoSSe, XZnAZ$_2$ (X = Cl, Br, I; A = Al, Ga, In; Z = S, Se), M$_2$CTT′ (M = Y, Sc; T/T′ = Br, Cl, F) MXenes, and XAu$_4$Y (X, Y = S, Se, Te; X ≠ Y), these Janus monolayers demonstrate superior absorption behaviour in the relevant spectral range.[58,75–78]

Among the two, SeGa–PbP shows a slightly enhanced absorption profile in most of the visible and near-UV range. This improvement is related to the altered electronic structure induced by replacing S with Se, which modifies the probabilities of optical transition and strengthens light–matter coupling.

3.5 The photocatalytic activity of XGa–PbP Janus monolayers

To efficiently drive the photocatalytic splitting of water into hydrogen and oxygen, the photocatalyst must exhibit suitable band-edge positions.[79,80] Specifically, CBM should be above the reduction potential of H$^+$/H$_2$, while the VBM should be below the oxidation potential of O$_2$/H$_2$O. These energetic criteria ensure that photoexcited electrons and holes possess sufficient

Table 3 Summary of electronic and photocatalytic properties: HSE06 band gap (E_g), effective masses (m_e^*/m_h^*), separation efficiency (R), work function (ϕ), electrostatic potential difference ($\Delta\phi$), redox potentials for H$_2$ and O$_2$ evolution (χ_{H_2} and χ_{O_2} at pH = 7), light absorption efficiency (η_{abs}), carrier utilisation rate (η_{cu}), solar-to-hydrogen efficiency (η_{STH}), corrected STH efficiency (η'_{STH}) of SGa–PbP and SeGa–PbP Janus monolayers

System	E_g^{HSE} (eV)	$m_e^*/m_h^*(m_0)$	R	ϕ (eV)	$\Delta\phi$ (eV)	χ_{H_2} (eV)	χ_{O_2} (eV)	η_{abs} (%)	η_{cu} (%)	η_{STH} (%)	η'_{STH} (%)
SGa–PbP	0.93	0.25/0.58	2.32	5.12/4.70	0.42	0.04	0.09	88.70	55.86	49.55	40.69
SeGa–PbP	1.24	0.19/0.59	3.10	5.24/4.58	0.66	0.57	0.11	74.03	53.57	39.66	31.75

potential to initiate the hydrogen and oxygen evolution reactions, respectively.

Importantly, the redox potentials of water depend on the pH of the environment. Under standard conditions (pH = 0), the redox potential for the hydrogen evolution reaction (H⁺/H₂) is defined as:

$$E_{H^+/H_2} = -4.44 \text{ eV} + (0.059 \text{ eV}) \times \text{pH} \qquad (6)$$

Similarly, the redox potential for the oxygen evolution reaction (O₂/H₂O) is:

$$E_{O2/H_2O} = -5.67 \text{ eV} + (0.059 \text{ eV}) \times \text{pH} \qquad (7)$$

Under neutral conditions (pH = 7), these values become −4.02 eV for H⁺/H₂ and −5.25 eV for O₂/H₂O, respectively. For a material to act as an efficient photocatalyst, its CBM should lie above (more negative than) −4.02 eV, and its VBM should lie below (more positive than) −5.25 eV at pH 7.

To determine the band alignment of the studied Janus monolayers, we first calculate the work function (ϕ), which is defined as the energy difference between the vacuum and Fermi levels as follows:

$$\phi = V_{vacuum} - E_{Fermi} \qquad (8)$$

The computed ϕ values for the Janus SGa–PbP and SeGa–PbP monolayers are summarised in Fig. 5 and Table 3. A notable asymmetry is observed in the work functions across the two opposite surfaces of each structure. This disparity originates from the inherent lack of mirror symmetry in the Janus architecture, which introduces a built-in dipole moment perpendicular to the plane of the monolayer (along the z-axis). Consequently, an internal electric field is established, oriented from the P-terminated surface toward the chalcogen-terminated side (X = S, Se).

This compositional asymmetry also leads to a pronounced modulation in the electrostatic potential distribution across the monolayer thickness. The computed electrostatic potential differences ($\Delta\phi$) are 0.42 eV for SGa–PbP and 0.66 eV for SeGa–PbP, indicating the presence of an intrinsic electric field, which is more prominent in the SeGa–PbP system.

Fig. 6 presents the band edge alignment of Janus SGa–PbP and SeGa–PbP monolayers, with the CBM and VBM referenced to the vacuum level on both the X- and P-terminated surfaces at pH = 0, 7, and 14. At neutral pH = 7, both materials exhibit a complete straddling of the water redox potentials, enabling simultaneous hydrogen evolution reaction and oxygen evolution reaction. Under acidic conditions (pH = 0), their band edges shift such that they only favor OER while HER becomes energetically inaccessible, whereas in alkaline conditions (pH = 14), the alignment permits only HER without supporting OER.

For SGa–PbP at neutral pH (pH = 7), the VBM on the P-terminated side is located at −4.92 eV, which lies above the water oxidation potential (−5.25 eV), suggesting that this side is not favourable for oxygen evolution. In contrast, the VBM on the S-terminated side drops to −5.34 eV, making it energetically suitable for the oxidation half-reaction. The corresponding CBM on the S side is situated at −3.98 eV, slightly above the reduction potential of hydrogen (−4.02 eV), thus enabling HER.

A comparable behavior is found for the SeGa–PbP monolayer under the same neutral conditions. Here, the VBM shifts from −4.70 eV on the P-terminated side to −5.36 eV on the Se-terminated side, indicating greater suitability for oxygen evolution on the Se side. Furthermore, the CBM on the P-terminated surface is located at −3.45 eV, well above the hydrogen evolution threshold, confirming that this side can
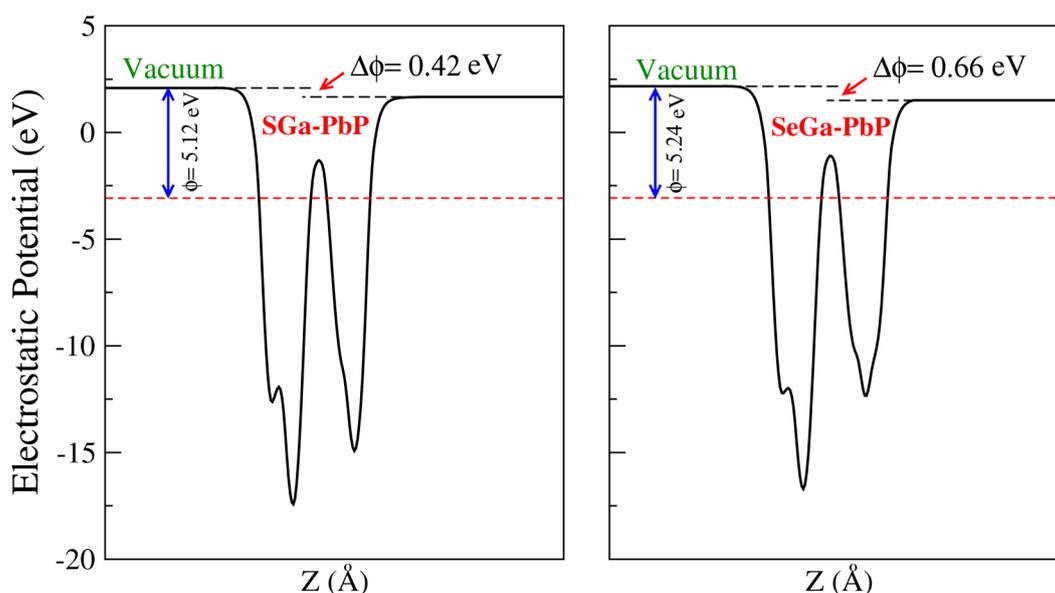

Fig. 5 Planar-averaged electrostatic potential of the SGa–PbP and SeGa–PbP Janus monolayers along the z-axis. The potential difference, denoted as ($\Delta\phi$), reflects the asymmetry between the two surfaces.
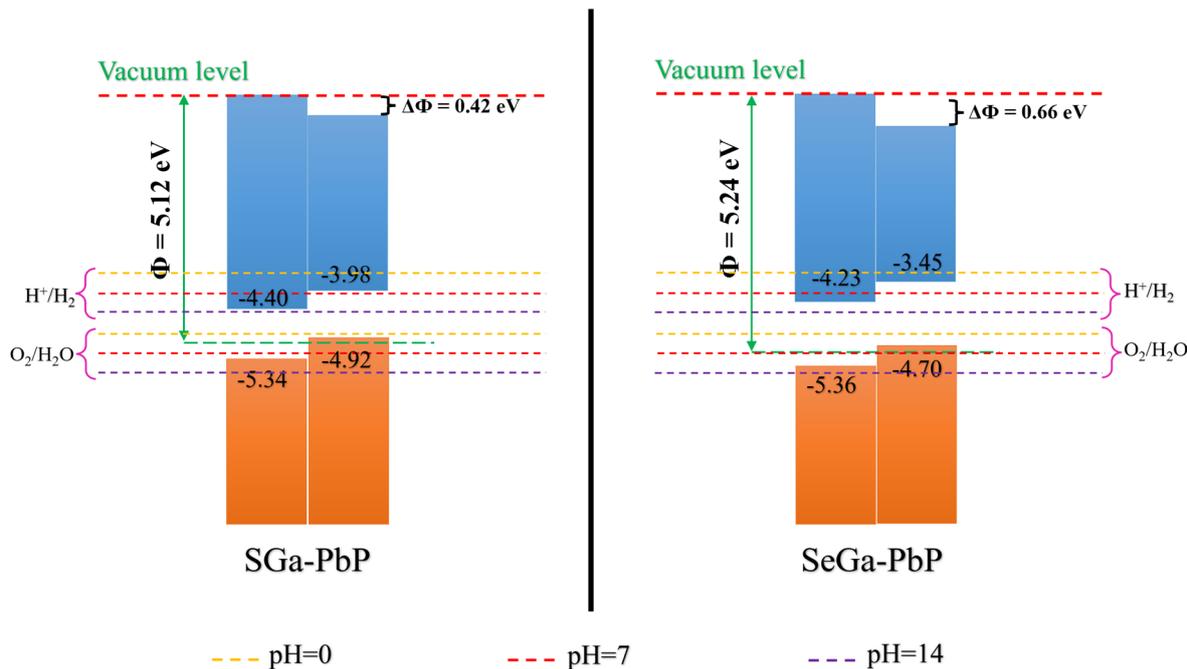
Fig. 6 Calculated band edge positions of the SGa–PbP and SeGa–PbP Janus monolayers with respect to the vacuum level. The redox potentials for hydrogen evolution (H⁺/H₂) and oxygen evolution (O₂/H₂O) at pH = 0, 7 and 14.

efficiently drive HER. These asymmetric band alignments highlight the intrinsic capability of Janus monolayers to spatially separate redox reactions, a desirable feature for efficient photocatalytic water splitting.

3.5.1 Hydrogen evolution reaction performance. The Gibbs free energy change for hydrogen adsorption (ΔG_{H*}), a widely accepted descriptor to evaluate HER activity, was calculated for the SGa–PbP and SeGa–PbP monolayers. This thermodynamic parameter is defined as:[81–83]

$$\Delta G_{H*} = \Delta E_{H*} + \Delta E_{ZPE} - T\Delta S \quad (9)$$

Here, ΔE_{H*}, ΔE_{ZPE}, and ΔS denote, respectively, the hydrogen binding strength, the variation in zero-point energy, and the change in entropy between the adsorbed H atom and the hydrogen gas under standard conditions.

The adsorption energy of a single hydrogen atom on the XGa–PbP surfaces is calculated using the following expression:

$$E_{ads} = E_{monolayer+H} - E_{monolayer} - \tfrac{1}{2}E_{H2} \quad (10)$$

where $E_{monolayer+H}$ and $E_{monolayer}$ are the total energies of the monolayer with and without adsorbed hydrogen atom, respectively. The E_{H_2} is the total energy of a hydrogen molecule in the gas phase state.

Following established approaches in the literature, the ZPE and entropy contributions to the Gibbs free energy of hydrogen adsorption can be approximated as a constant correction of approximately 0.24 eV.[84] Specifically, the difference in ZPE between the adsorbed hydrogen atom and half of an H₂ molecule typically lies in the range of 0.02 to 0.04 eV. The entropy contribution is estimated using the approximation that the

entropy of an adsorbed hydrogen atom is negligible compared to that of molecular hydrogen. As a result, the entropy change is taken as half the standard entropy of the H₂ gas at 298 K, yielding a value of approximately 0.20 eV for the term $T\Delta S$. Summing these two contributions gives:[81]

$$\Delta G_{H*} \approx E_{ads} + 0.24 \quad (11)$$

Based on Sabatier's principle,[85] optimal catalytic performance for HER is achieved when the surface binds to hydrogen with moderate strength, reflected by a ΔG_{H*} value that approaches zero, indicating thermoneutral adsorption.

Since HER experiments are often conducted in electrolytes of varying pH, the influence of proton concentration must be taken into account. Based on the Nernst equation, the Gibbs free energy varies with pH according to:

$$\Delta G_{H*}(pH) = \Delta G_{H*}(0) + 0.059 \times pH \quad (12)$$

This relationship indicates that hydrogen adsorption becomes progressively less favorable as the pH increases, a factor that is particularly relevant when assessing catalyst performance under neutral or alkaline conditions.

To assess the hydrogen adsorption behaviour of the Janus SGa–PbP and SeGa–PbP monolayers, three representative adsorption sites were examined on each surface. On the bottom XGa side, the adsorption sites included the top of the Ga atom, the top of the X atom (X = S or Se), and the hollow site (HB) located between neighboring atoms. On the top PbP side, hydrogen was adsorbed at the top of the Pb atom, the P atom, and the corresponding hollow site (HT). These adsorption configurations are depicted in Fig. 7(a and b).
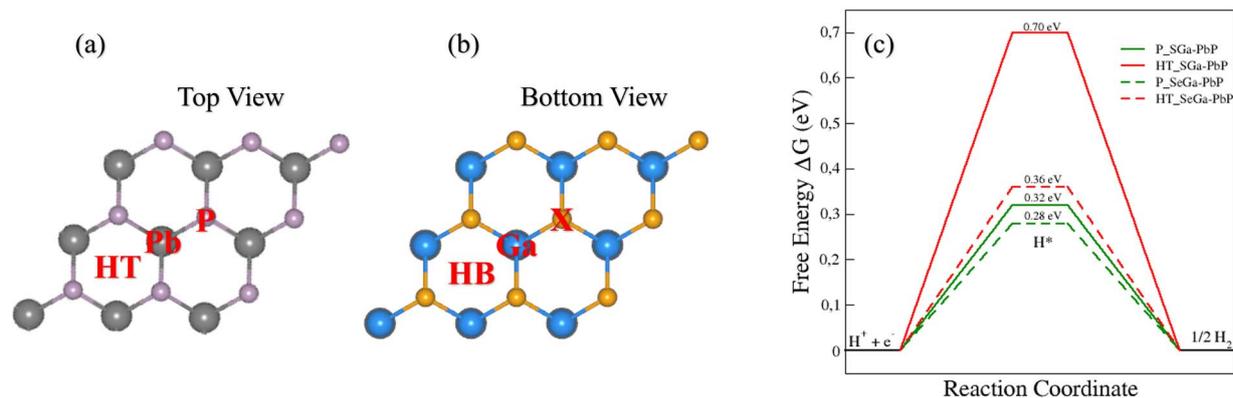
Fig. 7 (a and b) Possible hydrogen adsorption sites on the top and bottom surfaces of the Janus monolayers. (c) Gibbs free energy profiles for hydrogen adsorption for the most favorable sites of the SGa–PbP and SeGa–PbP Janus monolayers, illustrating the catalytic activity toward the HER.

All considered configurations were fully relaxed. Given that the studied monolayers can perform overall water splitting under neutral pH, the evaluation of Gibbs free energy at this condition was carried out. The corresponding adsorption energies and Gibbs free energies for hydrogen adsorption were then computed at pH = 7, and a summary of the results is provided in Table 4.

For the SGa–PbP monolayer, the P site exhibits the most favourable adsorption energy with a $\Delta G_{H*}(7)$ value of 0.32 eV, closely the thermoneutral condition. The hollow site (HT) also shows moderate catalytic performance with a value of 0.70 eV. In contrast, other adsorption sites on the SGa surface yield significantly higher $\Delta G_{H*}(7)$ values, indicating weak hydrogen binding (see Fig. 7(c)).

Similarly, in the SeGa–PbP monolayer, the most active HER sites are located on the PbP side, with $\Delta G_{H*}(7)$ values of 0.28 eV at the P site and 0.36 eV at the HT site. In contrast, the SeGa surface exhibits consistently larger $\Delta G_{H*}(7)$ values, suggesting limited HER activity due to weak H binding. These results highlight the PbP surface as the catalytically active facet for hydrogen evolution in both Janus systems, in agreement with

the charge transfer and electronic characteristics discussed earlier (see Fig. 7(c)).

Notably, the obtained ΔG_{H*} values are comparable to those reported for AlS (1.24 eV) and Al₂OS (0.97 eV),[86] and significantly better than those of MoSSe, MoSeTe, and MoSTe, which exhibit higher values of 2.04, 2.17, and 2.29 eV, respectively.[87,88]

3.5.2 Solar to hydrogen efficiency. The ultimate aim of solar-driven photocatalytic water splitting is to maximize the efficiency of solar-to-hydrogen (STH) energy conversion. Following the approach proposed by Fu et al.,[21] we evaluated the theoretical efficiency of the STH of the examined Janus monolayers. Assuming ideal catalytic conditions, this method defines the STH efficiency (η_{STH}) as the product of two factors: the light absorption efficiency (η_{abs}) and the carrier utilisation efficiency (η_{cu}):

$$\eta_{STH} = \eta_{abs} \times \eta_{cu} \tag{13}$$

The light absorption efficiency is expressed as the ratio of the solar power absorbed above the bandgap (E_g) to the total incident solar power:

$$\eta_{abs} = \frac{\int_{E_g}^{\infty} P(\hbar\omega)\mathrm{d}(\hbar\omega)}{\int_0^{\infty} P(\hbar\omega)\mathrm{d}(\hbar\omega)} \tag{14}$$

The carrier utilisation efficiency accounts for the fraction of absorbed photons that effectively contribute to the water splitting reaction:

$$\eta_{cu} = \frac{\Delta G \int_E^{\infty} \frac{P(\hbar\omega)}{\hbar\omega}\mathrm{d}(\hbar\omega)}{\int_{E_g}^{\infty} P(\hbar\omega)\mathrm{d}(\hbar\omega)} \tag{15}$$

Here, $\hbar\omega$ denotes the photon energy, and $P(\hbar\omega)$ is the solar spectral irradiance under the AM1.5G standard. The quantity ΔG represents the minimum thermodynamic potential (1.23 eV) needed to drive the water splitting, while E is the minimum effective photon energy accounting for overpotentials.

Table 4 Adsorption energy (E_{ads}) and Gibbs free energy ($\Delta G_{(H*)}$) for different adsorption sites

	Site	E_{ads} (eV)	$\Delta G_{(H*)}(7)$ (eV)
SGa–PbP	S	0.75	1.40
	Ga	0.33	0.98
	HB	0.73	1.38
	Pb	1.22	1.87
	P	−0.33	0.32
	HT	0.05	0.70
SeGa–PbP	Se	1.00	1.65
	Ga	0.73	1.38
	HB	1.03	1.68
	Pb	1.31	1.96
	P	−0.37	0.28
	HT	−0.29	0.36

To realistically estimate the STH efficiency, it is essential to account for energy losses arising from the overpotentials associated with the HER and the OER. These overpotentials are the result of kinetic barriers and interfacial carrier migration inefficiencies, and are typically approximated as 0.2 eV for HER and 0.6 eV for OER. Taking these into account, the effective energy available for driving the water splitting, indicated by E, is determined using the following conditional formulation:[21]

$$
E = \begin{cases}
E_g & (\chi_{H_2} \geq 0.2, \ \chi_{O_2} \geq 0.6) \\
E_g + 0.2 - \chi_{H_2} & (\chi_{H_2} < 0.2, \ \chi_{O_2} \geq 0.6) \\
E_g + 0.6 - \chi_{O_2} & (\chi_{H_2} \geq 0.2, \ \chi_{O_2} < 0.6) \\
E_g + 0.8 - \chi_{H_2} - \chi_{O_2} & (\chi_{H_2} < 0.2, \ \chi_{O_2} < 0.6)
\end{cases}
\tag{16}
$$

All necessary integrals were evaluated using a custom Python script, to obtain the final STH efficiency values.

An improvement of the catalytic performance of Janus 2D materials arises from their built-in transversal electric fields, which significantly aid in separating photogenerated charge carriers. This intrinsic electric field reduces the probability of recombination and improves the overall performance of the STH. To reflect this contribution, a corrected STH efficiency (η'_{STH}) is introduced:[21]

$$
\eta'_{STH} = \eta_{STH} \times \frac{\int_0^\infty P(\hbar\omega), d(\hbar\omega)}{\int_0^\infty P(\hbar\omega), d(\hbar\omega) + \Delta\phi \int_{E_g}^\infty \frac{P(\hbar\omega)}{\hbar\omega}, d(\hbar\omega)}
\tag{17}
$$

In this expression, $\Delta\phi$ denotes the potential difference between the vacuum levels on opposite sides of the Janus structure, effectively representing the influence of the internal electric field. This correction ensures a more accurate estimation of photocatalytic performance in materials with intrinsic asymmetry. The calculated values of η_{STH} and η'_{STH} for the investigated monolayers are summarised in Table 3.

As discussed previously, the Janus monolayers SGa–PbP and SeGa–PbP exhibit strong light absorption across both the visible and ultraviolet regions of the spectrum. Consequently, the light absorption efficiency (η_{abs}) reaches remarkable values of 88.70% for SGa–PbP and 74.03% for SeGa–PbP. In addition, the effective separation of electron–hole pairs and the enhanced mobility of charge carriers contribute to high charge carrier utilisation efficiencies (η_{cu}) of 55.86% for SGa–PbP and 53.57% for SeGa–PbP. The solar-to-hydrogen conversion efficiency (η_{STH}) and its corrected value (η'_{STH}) are calculated to be 49.55% and 40.69%, respectively, for the SGa–PbP monolayer, while SeGa–PbP achieves 39.66% and 31.75%, respectively.

When comparing the two monolayers, SGa–PbP consistently outperforms SeGa–PbP in all evaluated metrics, confirming its superior potential for solar-driven hydrogen production. The observed η_{STH} values for XGa–PbP also exceed those of several previously reported Janus monolayers, such as MoSSe (17.14% (ref. 89)), n-BSb (17.20% (ref. 90)), and SAu6Se (23.55% (ref. 91)), highlighting their strong intrinsic photocatalytic capability. Notably, the corrected η'_{STH} values of Janus XGa–PbP

monolayers also surpass the commercial benchmark of 10%, and outperform those of several recently reported Janus monolayers, including MoSSe (20.39% (ref. 92)), BAsS (33.93% (ref. 93)), and CrSSnN$_2$ (36.78% (ref. 94)). These results collectively position XGa–PbP Janus monolayers among the most efficient and promising candidates for photocatalytic hydrogen generation.

4 Conclusion

In summary, we have proposed and systematically explored two novel Janus monolayers, SGa–PbP and SeGa–PbP, through first-principles calculations. Our study reveals that the studied Janus monolayers possess strong stability, supported by their favourable energetics, dynamic behavior, thermodynamics, and mechanical properties. Both materials are direct band gap semiconductors, with band gaps of 0.93 eV and 1.24 eV, falling within the ideal range for visible-light-driven photocatalysis, complemented by robust optical absorption in the visible and ultraviolet regions, making them promising for optoelectronic and energy applications. Moreover, both Janus monolayers exhibit promising photocatalytic properties, with conduction band-edge positions suitably aligned above the hydrogen evolution potential. Additionally, hydrogen adsorption analysis reveals that the PbP surface hosts the most active catalytic sites, further confirming their potential for efficient HER applications. The calculated and corrected solar-to-hydrogen (STH) conversion efficiencies are found to be 49.55% (40.69% after correction) for SGa–PbP and 39.66% (31.75% corrected) for SeGa–PbP, exceeding several previously reported 2D materials. These results expand the repertoire of functional two-dimensional Janus materials and highlight the significant potential of SGa–PbP and SeGa–PbP in the advancement of next-generation photocatalytic water-splitting technologies for sustainable hydrogen production. We advocate for future experimental efforts to synthesize these monolayers, focusing on validating their stability and efficiency under operating conditions, which could pave the way for their practical implementation.

Conflicts of interest

There are no conflicts to declare.

Data availability

The data of this study are available from the corresponding author upon reasonable request.

Supplementary Fig. S1 presents the band structures of SGa–PbP and SeGa–PbP monolayers calculated with PBE and PBE + SOC. Table S1 summarizes the corresponding band gaps (E_g) and the differences (ΔE_g) between both methods. See DOI: **https://doi.org/10.1039/d5ra04300j**.

Acknowledgements

References

1 S. B. Pillai, B. A. Baraiya, D. Upadhyay, V. Mankad and P. K. Jha, *Int. J. Hydrogen Energy*, 2020, **45**, 23900–23907.

2 M. H. Dalsaniya, T. K. Gajaria, N. N. Som and P. K. Jha, *Phys. Chem. Chem. Phys.*, 2020, **22**, 19823–19836.

3 D. Chodvadiya, N. N. Som, P. K. Jha and B. Chakraborty, *Int. J. Hydrogen Energy*, 2021, **46**, 22478–22498.

4 W. Hao, J. Fan, X. Xu, Y. Zhang, H. Lv, S. Wang, S. Deng, S. Weng and Y. Guo, *Dalton Trans.*, 2021, **50**, 13312–13319.

5 W. Hao, D. Yao, Q. Xu, R. Wang, C. Zhang, Y. Guo, R. Sun, M. Huang and Z. Chen, *Appl. Catal., B*, 2021, **292**, 120188.

6 A. J. Morris, G. J. Meyer and E. Fujita, *Acc. Chem. Res.*, 2009, **42**, 1983–1994.

7 G. Palmisano, E. García-López, G. Marcì, V. Loddo, S. Yurdakal, V. Augugliaro and L. Palmisano, *Chem. Commun.*, 2010, **46**, 7074–7089.

8 Q. Zhang, X. Wang and S. Yang, *ACS Appl. Mater. Interfaces*, 2021, **13**, 31934–31946.

9 Y. Yu, J. Zhou, Z. Guo and Z. Sun, *ACS Appl. Mater. Interfaces*, 2021, **13**, 28090–28097.

10 A. Fujishima and K. Honda, *Nature*, 1972, **238**, 37–38.

11 S. U. Khan, M. Al-Shahry and W. B. Ingler Jr, *Science*, 2002, **297**, 2243–2245.

12 Z. Ma, K. Wu, R. Sa, Q. Li, C. He and Z. Yi, *Int. J. Hydrogen Energy*, 2015, **40**, 980–989.

13 S. Cao and J. Yu, *J. Phys. Chem. Lett.*, 2014, **5**, 2101–2107.

14 Z. Ma, Z. Yi, J. Sun and K. Wu, *J. Phys. Chem. C*, 2012, **116**, 25074–25080.

15 H. Kato, K. Asakura and A. Kudo, *J. Am. Chem. Soc.*, 2003, **125**, 3082–3089.

16 A. K. Geim and K. S. Novoselov, *Nat. Mater.*, 2007, **6**, 183–191.

17 D. Fan, M. Yin, X. Tan, H. Li, H. Hu, Z. Nie, F. Guo, Z. Feng, J. Li, Z. Wang, *et al.*, *Int. J. Hydrogen Energy*, 2025, **112**, 493–502.

18 Y. Ren, X. Ma, G. Yuan, J. Liao, N. Ma, D. Li and H. Lv, *Phys. Chem. Chem. Phys.*, 2024, **26**, 16765–16773.

19 G. Yuan, X. Ma, J. Liao, T. Xie, Q. Xie and Z. Yuan, *ACS Appl. Nano Mater.*, 2023, **6**, 1956–1964.

20 L. Wang, Y. Zhang, L. Chen, H. Xu and Y. Xiong, *Adv. Mater.*, 2018, **30**, 1801955.

21 C.-F. Fu, J. Sun, Q. Luo, X. Li, W. Hu and J. Yang, *Nano Lett.*, 2018, **18**, 6312–6317.

22 T. Yu, C. Wang, X. Yan, G. Yang and U. Schwingenschlogl, *J. Phys. Chem. Lett.*, 2021, **12**, 2464–2470.

23 D. Gu, X. Tao, H. Chen, W. Zhu, Y. Ouyang and Q. Peng, *Nanoscale*, 2019, **11**, 2335–2342.

24 C. Xia, W. Xiong, J. Du, T. Wang, Y. Peng and J. Li, *Phys. Rev. B*, 2018, **98**, 165424.

25 P. Nandi, A. Rawat, R. Ahammed, N. Jena and A. De Sarkar, *Nanoscale*, 2021, **13**, 5460–5478.

26 J. Fan, W. Hao, C. Fu, Z. Chen, R. Liang, C. Lian, Q. Zhang and G. Li, *J. Mater. Chem. A*, 2022, **10**, 1535–1546.

27 A.-Y. Lu, H. Zhu, J. Xiao, C.-P. Chuu, Y. Han, M.-H. Chiu, C.-C. Cheng, C.-W. Yang, K.-H. Wei, Y. Yang, *et al.*, *Nat. Nanotechnol.*, 2017, **12**, 744–749.

28 M. Sun and U. Schwingenschlogl, *Chem. Mater.*, 2020, **32**, 4795–4800.

29 H. Yang, P. Zhao, Y. Ma, X. Lv, B. Huang and Y. Dai, *J. Phys. D: Appl. Phys.*, 2019, **52**, 455303.

30 H. L. Zhuang and R. G. Hennig, *Chem. Mater.*, 2013, **25**, 3232–3238.

31 J.-H. Lin, H. Zhang, X.-L. Cheng and Y. Miyamoto, *Phys. Rev. B*, 2017, **96**, 035438.

32 Y. Hu, T. Li, L. Liu, Y. Tan, L. Hu, K. Wu and C. Yang, *Phys. B*, 2020, **594**, 412366.

33 X. Deng, W. Zhang, X. Zhou, Z. Wang, J. Tang, L. Hu, Y. Feng, K. Wu and C. Yang, *Int. J. Hydrogen Energy*, 2021, **46**, 35271–35279.

34 D. Wang, F. Luo, M. Lu, X. Xie, L. Huang and W. Huang, *Small*, 2019, **15**, 1804404.

35 X. Zhang, J. Kang, K. H. Choi, J. Jeon, B. J. Jeong, H.-S. Bang, H.-S. Oh, J. Lim, J.-H. Park, J.-H. Lee, *et al.*, *Chem. Mater.*, 2024, **36**, 2533–2543.

36 J. Jeon, S. K. Jang, S. M. Jeon, G. Yoo, Y. H. Jang, J.-H. Park and S. Lee, *Nanoscale*, 2015, **7**, 1688–1695.

37 M. Gu, C. Li, Y. Ding, K. Zhang, S. Xia, Y. Wang, M.-H. Lu, H. Lu and Y.-F. Chen, *Appl. Sci.*, 2020, **10**, 639.

38 B. Hu, F. Cai, T. Chen, M. Fan, C. Song, X. Yan and W. Shi, *ACS Appl. Mater. Interfaces*, 2015, **7**, 18247–18256.

39 P. Hu, L. Wang, M. Yoon, J. Zhang, W. Feng, X. Wang, Z. Wen, J. C. Idrobo, Y. Miyamoto, D. B. Geohegan, *et al.*, *Nano Lett.*, 2013, **13**, 1649–1654.

40 L. Liu, C. Yan, L. Gao, W. Shangguan, J. Dai and J. Cai, *Mater. Res. Express*, 2021, **8**, 125010.

41 G. Kresse and J. Hafner, *Phys. Rev. B: Condens. Matter Mater. Phys.*, 1993, **48**, 13115.

42 G. Kresse and J. Furthmüller, *Phys. Rev. B: Condens. Matter Mater. Phys.*, 1996, **54**, 11169.

43 M. Ernzerhof and G. E. Scuseria, *J. Chem. Phys.*, 1999, **110**, 5029–5036.

44 S. Grimme, *J. Comput. Chem.*, 2006, **27**, 1787–1799.

45 P. E. Blöchl, *Phys. Rev. B: Condens. Matter Mater. Phys.*, 1994, **50**, 17953.

46 J. Heyd, G. E. Scuseria and M. Ernzerhof, *J. Chem. Phys.*, 2003, **118**, 8207–8215.

47 M. Gajdoš, K. Hummer, G. Kresse, J. Furthmüller and F. Bechstedt, *Phys. Rev. B: Condens. Matter Mater. Phys.*, 2006, **73**, 045112.

48 S. Grimme, S. Ehrlich and L. Goerigk, *J. Comput. Chem.*, 2011, **32**, 1456–1465.

49 L. Chaput, A. Togo, I. Tanaka and G. Hug, *Phys. Rev. B: Condens. Matter Mater. Phys.*, 2011, **84**, 094302.

50 A. Togo, L. Chaput, T. Tadano and I. Tanaka, *J. Phys.: Condens. Matter*, 2023, **35**, 353001.

51 A. Togo, *J. Phys. Soc. Jpn.*, 2023, **92**, 012001.

52 S. Nosé, *Mol. Phys.*, 1984, **52**, 255–268.

53 W. G. Hoover, *Phys. Rev. A*, 1985, **31**, 1695.

54 V. Wang, N. Xu, J.-C. Liu, G. Tang and W.-T. Geng, *Comput. Phys. Commun.*, 2021, **267**, 108033.

55 K. Momma and F. Izumi, *J. Appl. Crystallogr.*, 2008, **41**, 653–658.

56 S. Soleimani-Amiri, N. Ghobadi, A. Rezavand and S. G. Rudi, *Appl. Surf. Sci.*, 2023, **623**, 157020.

57 A. Rezavand and N. Ghobadi, *Mater. Sci. Semicond. Process.*, 2022, **152**, 107061.

58 Y. Zou, B. Sun, J. Li, L. Zhao, C. Kou, M. Zhang and Y. Tian, *Appl. Surf. Sci.*, 2025, **693**, 162806.

59 K. Chaoui, W. Elaggoune and K. Zanat, *Int. J. Hydrogen Energy*, 2024, **91**, 1221–1231.

60 M. Born and K. Huang, *Dynamical Theory of Crystal Lattices*, Clarendon Press, Oxford, 1954.

61 F. Mouhat and F.-X. Coudert, *Phys. Rev. B: Condens. Matter Mater. Phys.*, 2014, **90**, 224104.

62 V. Van Thanh, N. T. Hung, *et al.*, *Phys. Chem. Chem. Phys.*, 2019, **21**, 22377–22384.

63 E. Cadelano, P. L. Palla, S. Giordano and L. Colombo, *Phys. Rev. B: Condens. Matter Mater. Phys.*, 2010, **82**, 235414.

64 J. Heyd, G. E. Scuseria and M. Ernzerhof, *J. Chem. Phys.*, 2003, **118**, 8207–8215.

65 K. Chaoui, K. Zanat, W. Elaggoune, L. Henrard and M. Achehboune, *RSC Adv.*, 2024, **14**, 39625–39635.

66 D. Fan, M. Yin, K. Wang, Z. Wang, H. Li, H. Hu, F. Guo, Z. Feng, J. Li, D. Zhang, *et al.*, *Int. J. Hydrogen Energy*, 2025, **107**, 452–459.

67 P. Borlido, J. Doumont, F. Tran, M. A. Marques and S. Botti, *J. Chem. Theory Comput.*, 2020, **16**, 3620–3627.

68 A. Marrazzo and N. Colonna, *Phys. Rev. Res.*, 2024, **6**, 033085.

69 P.-P. Sun, Q.-S. Li, L.-N. Yang and Z.-S. Li, *Nanoscale*, 2016, **8**, 1503–1512.

70 W. P. Huhn and V. Blum, *Phys. Rev. Mater.*, 2017, **1**, 033803.

71 F. Opoku, K. K. Govender, C. G. C. E. vanSittert and P. P. Govender, *ChemistrySelect*, 2017, **2**, 6304–6316.

72 L. Thulin and J. Guerra, *Phys. Rev. B: Condens. Matter Mater. Phys.*, 2008, **77**, 195112.

73 W. Yu, D. Xu and T. Peng, *J. Mater. Chem. A*, 2015, **3**, 19936–19947.

74 M. Gajdoš, K. Hummer, G. Kresse, J. Furthmüller and F. Bechstedt, *Phys. Rev. B: Condens. Matter Mater. Phys.*, 2006, **73**, 045112.

75 R. Chaurasiya, G. K. Gupta and A. Dixit, *Sol. Energy Mater. Sol. Cells*, 2019, **201**, 110076.

76 M. Idrees, H. Din, R. Ali, G. Rehman, T. Hussain, C. Nguyen, I. Ahmad and B. Amin, *Phys. Chem. Chem. Phys.*, 2019, **21**, 18612–18621.

77 B. D. Aparicio-Huacarpuma, M. L. Pereira Junior, A. M. Silva, A. C. Dias and L. A. Ribeiro Junior, *ACS Appl. Energy Mater.*, 2025, **8**, 6634–6644.

78 D.-Q. Xie, L. Liu and H.-Z. Guo, *Sol. Energy*, 2025, **285**, 113149.

79 D. Fan, Z. Wang, M. Yin, H. Li, H. Hu, F. Guo, Z. Feng, J. Li, D. Zhang, M. Zhu, *et al.*, *Phys. B*, 2024, **673**, 415486.

80 D. Fan, M. Yin, F. Wang, Z. Wang, H. Li, H. Hu, F. Guo, Z. Feng, J. Li, D. Zhang, *et al.*, *Int. J. Hydrogen Energy*, 2024, **60**, 342–353.

81 J. K. Nørskov, T. Bligaard, A. Logadottir, J. Kitchin, J. G. Chen, S. Pandelov and U. Stimming, *J. Electrochem. Soc.*, 2005, **152**, J23.

82 J. Greeley, T. F. Jaramillo, J. Bonde, I. Chorkendorff and J. K. Nørskov, *Nat. Mater.*, 2006, **5**, 909–913.

83 H.-H. Wu, H. Huang, J. Zhong, S. Yu, Q. Zhang and X. C. Zeng, *Nanoscale*, 2019, **11**, 12210–12219.

84 P. J. Linstrom and W. G. Mallard, *J. Chem. Eng. Data*, 2001, **46**, 1059–1063.

85 P. Sabatier, *Ber. Dtsch. Chem. Ges.*, 1911, **44**, 1984–2001.

86 Z. Haman, N. Khossossi, M. Kibbou, I. Bouziani, D. Singh, I. Essaoudi, A. Ainane and R. Ahuja, *Appl. Surf. Sci.*, 2022, **589**, 152997.

87 G. Liu, J. Peng, B. Jia, J. Hao, Z. Zhao, X. Ma, W. Zou and P. Lu, *Int. J. Hydrogen Energy*, 2023, **48**, 13902–13912.

88 F. Zhao, J. Li, Y. Chen, M. Zhang and H. Zhang, *Appl. Surf. Sci.*, 2021, **544**, 148741.

89 L. Ju, M. Bie, J. Shang, X. Tang and L. Kou, *J. Phys.: Mater.*, 2020, **3**, 022004.

90 W. Elaggoune, Y. Z. Abdullahi and K. Chaoui, *Int. J. Hydrogen Energy*, 2025, **156**, 150099.

91 Y. Tian, L. Gao, Y. Xue, W. Ren, X. Shai, H. Bai, C. Zeng and H. Wang, *ACS Appl. Nano Mater.*, 2024, **7**, 12848–12858.

92 F. Yang, M.-C. Record and P. Boulet, *Renewable Energy*, 2025, **245**, 122829.

93 Y. Zhao, B. Zhang and J. Lin, *Sol. Energy*, 2025, **288**, 113320.

94 L. Li, Y. Wang, Y. Wang, T. Chen, G. Wang, Z. Zhang, Z. Ding, X. Guo, Z. Luo and X. Liu, *Colloids Surf., A*, 2025, **705**, 135762.